Measurement of Effective Knudsen Diffusion Coefficients for Powder Beds Used in Heterogeneous Uptake Experiments

James E. Boulter[†] and Jochen Marschall*

Molecular Physics Laboratory, SRI International, 333 Ravenswood Avenue, Menlo Park, California 94025

Received: May 10, 2006; In Final Form: July 10, 2006

The effective Knudsen diffusion coefficients for characteristic oxide powder beds used in heterogeneous uptake experiments have been measured using countercurrent diffusion and transient pressure drop techniques. Room-temperature thermal-velocity-normalized effective Knudsen diffusion coefficients are found to lie in the 0.15 to 0.35 μm range for magnesium silicate, aluminum oxide, and iron oxide powder beds. Measured values are compared with theoretical estimates and are consistent with low bed tortuosities (below 3) expected for media with open porosity above 0.5. The impact of uncertainties in effective diffusion coefficients on corrections of measured uptake coefficients is discussed. The value of careful uptake measurements in both the low and high sample mass limits is reinforced, as this allows uptake corrections independent of explicitly measured or estimated diffusion coefficient values. It is suggested that correction procedures requiring tortuosity values greater than 3 are suspect.

1. Introduction

Some of the most compelling problems in the field of atmospheric chemistry are related to surface-mediated reactions. The best known of these is probably the catalytic conversion of photochemically inactive chlorine species to active chlorine species on the surfaces of polar stratospheric cloud particles, a process that contributes to stratospheric ozone depletion.[1−4] Other examples include the heterogeneous chemistries of nitrogen oxides on tropospheric aerosols[5] and trace atmospheric species on sea salt particles.[6−8]

Laboratory studies of heterogeneous chemistry rely on various techniques to quantify reaction rates. Techniques used extensively over the past years include flow tube reactors,[9−12] diffusion tube reactors,[13−20] and Knudsen cell reactors.[2−4,7,8,21−33] In these experimental techniques, changes in the gas-phase concentration of reactant and/or product species are measured as a gas mixture is exposed to a target surface.

The efficiency of a surface reaction can be characterized by an uptake coefficient, γ, defined as the fraction of surface collisions that result in loss of a reactant from the gas phase. Numerical values of γ are obtained by modeling measured changes in concentration with the appropriate coupled transport-chemistry model of the reactor. The reactor model will include the uptake coefficient and the sample surface area as part of the boundary conditions. In all cases, the numerical value assigned to γ ultimately depends on the estimate made for the true chemically participating surface area of the test specimen, A_t. Larger values of surface area will result in smaller values for the uptake coefficient and vice versa.

Even for nominally flat monolithic specimens, microscopic surface roughness can increase the chemically participating surface area well above the macroscopically measured geometric area.[17] The observed uptake coefficient, γ_o, can be defined as the value derived from experimental data using the observed (measured) geometric sample surface area, A_o. Since the geometric surface area is a lower bound on the true surface area ($A_o \leq A_t$), γ_o provides an upper bound on the true uptake coefficient ($\gamma_t \leq \gamma_o$). If A_t can be measured or estimated, a simple first-order approximation for the true uptake coefficient is

$$\gamma_t = \gamma_o \frac{A_o}{A_t} \tag{1}$$

Laboratory studies focused on heterogeneous atmospheric chemistry use surrogate materials for atmospheric particulates. If experiments can be performed on relatively large, solid, geometrically well-defined particles widely spaced on an inert surface, then the total reactive surface area and surface collision frequencies can be estimated directly from simple geometric and gas dynamic considerations. The Finlayson−Pitts research group has used this approach successfully to measure uptake coefficients on salt particles in a Knudsen cell reactor.[8] However, for many other materials and heterogeneous processes, it is difficult to make measurements using submonolayer samples. More typically, porous specimens have been used as surrogates for atmospheric particulates; for example, vapor-deposited ice films for ice particles[9,34,35] or oxide and mineral powder beds for dust particles.[26,30−33] In such cases, reactants penetrate the exposed outer boundary of the sample, reacting heterogeneously in-depth. Reactant loss is governed by a complicated diffusion-reaction process, whose details depend on the diffusion rate, the intrinsic surface reaction rate, and the accessible internal surface area of the sample.

For a porous sample, γ_o still provides an upper bound on γ_t. If A_t is taken as the total sample surface area measured by the BET (Brunauer, Emmett, and Teller) gas adsorption isotherm technique, eq 1 will return a lower bound on γ_t. Unfortunately, for samples with large internal surface areas, these two bounds can be separated by several orders of magnitude, a range much too large to usefully constrain uptake coefficients in atmospheric chemistry models.

This situation was recognized, and an improved correction procedure (the KML model) was introduced to the atmospheric

* To whom correspondence should be addressed. E-mail: jochen.marschall@sri.com.

[†] Present address: Chemistry Department, University of Wisconsin, Eau Claire, 105 Garfield Avenue, Eau Claire, WI 54702.

10.1021/jp062866i CCC: $33.50
Published on Web 08/15/2006

TABLE 1: Oxide Powder Characteristics

	Mg_2SiO_4	α-Al_2O_3	α-Fe_2O_3	γ-Fe_2O_3
supplier	Aesar	Aesar	Aldrich	Aesar
stock no.	43807	39814	31,0050	39951
lot no.	J10K11	I13L08	02808EA/09106KO	I27L05
purity, %	99	99.99	99+	99+
particle size, μm	< 44 (−325 mesh)	0.9−2.2	5	0.020−0.030
ρ_t, g cm^{-3}	3.21	3.97	5.24	5.18
ρ_b, g cm^{-3}	1.46	0.62	1.22	0.43
ϵ^a	0.54	0.84	0.77	0.92
S_{BET}, m^2 g^{-1}	0.77	9.5	4.3	41
r_p,^{b} μm	0.96	0.29	0.29	0.10

[a] Calculated from $\epsilon = 1 - \rho_b/\rho_t$. [b] Calculated from $r_p = 2\epsilon/\rho_b S_{BET}$.

chemistry community by Keyser et al.,[10] who studied reactions on vapor-deposited ice films in a flow tube apparatus. The KML model was adapted from a one-dimensional diffusion-reaction analysis developed in the chemical engineering community for describing reactions on porous pellets used in catalytic beds.[36,37] It was later modified by Underwood et al.[31] and applied to correct observed uptake coefficients measured on powder beds in a low-pressure Knudsen cell apparatus.

The KML approach is widely adopted and generally accepted as the best available correction procedure for porous samples. However, it remains very difficult to assess the accuracy of "true" uptake coefficients obtained in this manner. Uncertainties are introduced both by the limitations of a continuum diffusion-reaction model in describing the microphysical processes involved and by difficulties in assigning numerical values to various parameters in the model. Consequently, estimations of the chemically participating surface area, rather than the experimental measurement techniques themselves, remain the major source of uncertainty in reported uptake coefficients.

One of the central parameters in the KML model is the effective diffusion coefficient of the reactant gas in the porous sample. This quantity is not convenient to measure. A literature survey suggests that it has *never* been measured directly for ice or powder beds used in atmospheric heterogeneous chemistry experiments. In past work, the effective diffusion coefficient has been represented using gas kinetic theory and geometric information and either estimated[10,12,38] or used as a fitting parameter.[31]

In this paper, we report experimental measurements of the effective diffusion coefficients for several different oxide powder beds under low-pressure conditions. We examine powders with different particle sizes and shapes, leading to beds with different internal surface areas and porosities. Materials analyzed include magnesium silicate (Mg_2SiO_4), aluminum oxide (α-Al_2O_3), and iron oxide in two different crystalline forms (α-Fe_2O_3 and γ-Fe_2O_3).

In the sections that follow, we describe the oxide powders, review the KML model, describe our experimental approach, present the results of our measurements and discuss their ramifications for correcting observed uptake coefficients. We show that Knudsen diffusion is relatively fast in these powder beds, that bed tortuosities are low (~3 or less), and that a common approximation (twice the pore volume divided by the pore surface area) underestimates the characteristic pore size for diffusion. We suggest that independent diffusion coefficient measurements are not routinely required if careful uptake measurements are made in both the low and high sample mass limits, as these allow uptake corrections independent of explicitly measured or estimated diffusion coefficient values.

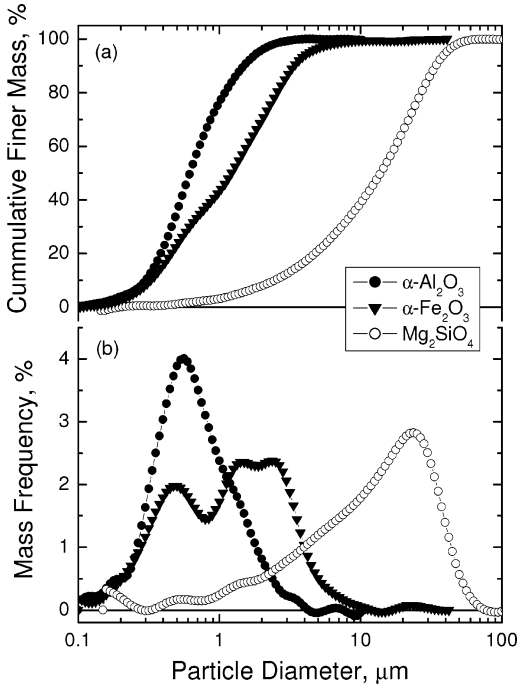

Figure 1. Particle size distributions measured by Stokes sedimentation for Mg_2SiO_4, α-Fe_2O_3, and α-Al_2O_3 powders.

2. Oxide Powders

Table 1 presents some characteristics of the oxide powders used in our experiments. All powders were commercially purchased and used as received without further processing. Three of these powders, α-Fe_2O_3, γ-Fe_2O_3, and α-Al_2O_3, have been used in Knudsen cell experiments reported by the Grassian research group[30−33] and were specifically chosen for study because of the excellent documentation of samples, experiments, and data analysis available in their publications, which greatly facilitates the interpretation of our findings.

Stock and lot numbers, sample purity, approximate particle size, and true material density were obtained from manufacturer specifications. Bulk densities were derived by measuring the mass and height of powder beds packed in a cylindrical holder of known diameter. The porosity ϵ is defined as the volume fraction of empty space in the powder bed and is calculated from $\epsilon = 1 - \rho_b/\rho_t$. Bulk density measurements, and hence the porosity values, were reproducible to within 8%. The porosity values that we measure for our α-Fe_2O_3 and α-Al_2O_3 beds differ by less than 3% from those given for the same materials by Underwood et al.[31]

Particle size distributions (Stokes sedimentation with X-ray absorption) and specific surface areas (multipoint N_2 BET adsorption isotherm) were performed by Micromeritics Instrument Corp., using instrumentation of their own manufacture. Since the oxide powder bed pore space is contiguous and open, BET adsorption measures the total pore surface area. Uncertainties in the BET measurements are reported as less than 0.5%, reflecting good fits between experimental data and the BET model. Compared with the values in Table 1, the BET surface areas reported by Underwood et al.[31,32] were higher by factors of 1.5 and 1.2 for α-Al_2O_3 and γ-Fe_2O_3 and lower by 0.42−0.54 for α-Fe_2O_3.

The characteristic pore dimension r_p is difficult to define precisely; a variety of different measures have been used including the radius of the average pore neck and the radius of the largest sphere that will fit inside an average pore. In Table 1, the characteristic pore dimension is calculated as twice the

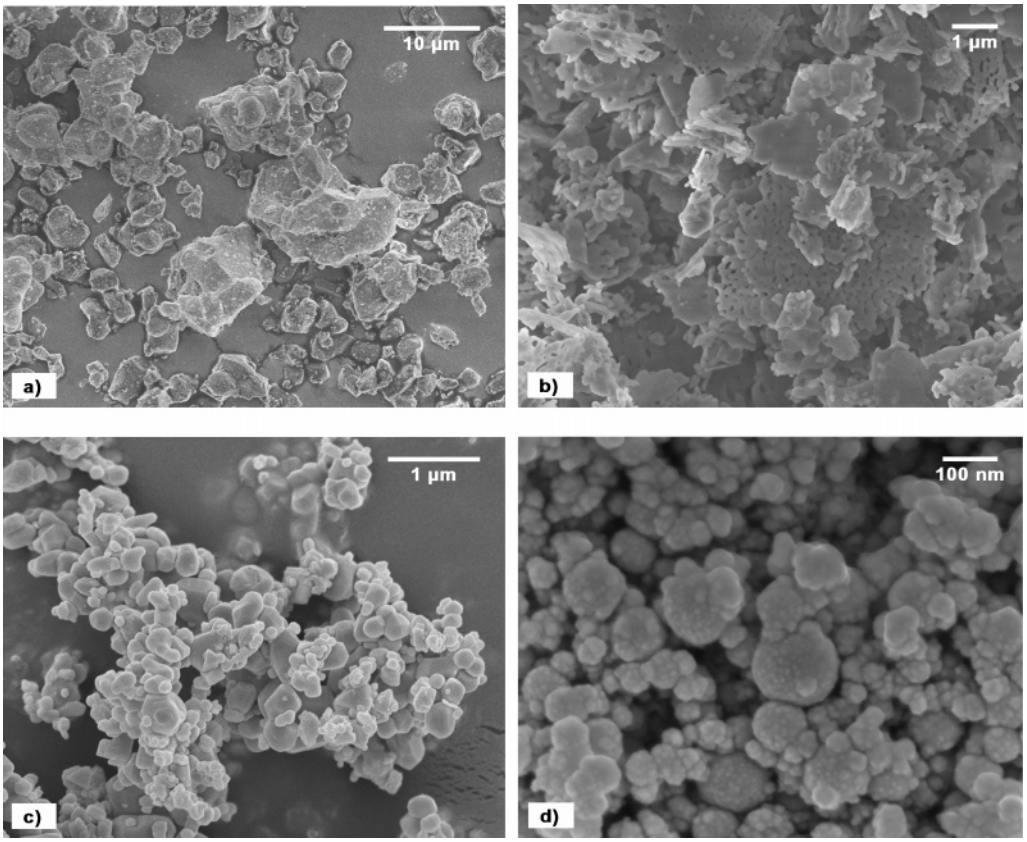

Figure 2. SEM images of oxide powders: (a) Mg_2SiO_4, (b) α-Al_2O_3, (c) α-Fe_2O_3, and (d) γ-Fe_2O_3.

pore volume divided by the pore surface area. This definition returns the tube radius, r_c, when applied to a single capillary tube, and allows for calculation of r_p from experimentally measured quantities using the relation $r_p = 2\epsilon/\rho_b S_{BET}$.

Figure 1 shows the particle size (effective spherical diameter) distributions measured for the Mg_2SiO_4, α-Fe_2O_3, and α-Al_2O_3 powders. Similar measurements were not possible for the very fine γ-Fe_2O_3 powders. The mass frequency distributions for Mg_2SiO_4 and α-Al_2O_3 are dominated by particle size modes near 24 and 0.55 μm, respectively, while the α-Fe_2O_3 distribution shows at least three modes of comparable strength at 0.49, 1.5, and 2.3 μm. The mean particles sizes are 16, 1.8, and 0.81 μm for Mg_2SiO_4, α-Fe_2O_3, and α-Al_2O_3, respectively. For a single material, the size distributions span 1 to 2 orders of magnitude, illustrating the difficulty in defining a meaningful "characteristic particle size" for a real powder bed.

Figure 2 shows scanning electron microscope (SEM) images of the four different powders. These images demonstrate that the spherical particle approximation is generally a gross simplification of the true particle geometry. This approximation does not accurately represent the geometry of the faceted, rock-like Mg_2SiO_4 particles or the nodular α-Fe_2O_3 particles and is completely inappropriate for the splintered, flake-like α-Al_2O_3 particles. Even for the γ-Fe_2O_3 powder which has the most spherical particles of the four powders, the SEM image reveals many particles that deviate strongly from this geometric approximation.

Figure 2c reveals that the intrinsic α-Fe_2O_3 particle sizes seem to fall in the ~100 s of nanometers range, suggesting that the larger particle size modes detected by Stokes sedimentation are actually agglomerates of smaller particles. Agglomeration may also explain the "5 μm" particle size given by the manufacture for this powder.

3. KML Model

In the KML model, the diffusion and first-order loss of a reactant in a porous sample is described by the one-dimensional steady-state diffusion-reaction equation

$$D_{eff}\frac{\partial^2 C}{\partial z^2} - kC = 0 \tag{2}$$

where D_{eff} is the effective diffusion coefficient of the reactant in porous media, C is the reactant concentration, and k is the reactant loss rate. The z-axis is taken as positive into the porous media, with $z = 0$ at the top surface exposed to the reactant gas. The reactant loss rate can be expressed as

$$k = \rho_b S_{BET}\frac{\gamma_t \bar{v}_p}{4} \tag{3}$$

where ρ_b is the bulk density of the porous sample, S_{BET} is the accessible pore surface area of the sample on a per mass basis as measured using BET absorption, and $\bar{v}_p = (8RT_p/\pi M)^{1/2}$, the thermal velocity of the reactant equilibrated to the temperature of the porous media, T_p, with R and M the universal gas constant and the reactant molar mass, respectively. For a sample of depth L, applying the boundary conditions

$$C(0) = C_0 \tag{4a}$$

and

$$D_{eff}\left.\frac{\partial C}{\partial z}\right|_L = 0 \tag{4b}$$

leads to the classic solution

$$C(z) = C_0 \frac{\cosh\left(\phi\left[1 - \frac{z}{L}\right]\right)}{\cosh(\phi)} \quad (5)$$

where $\phi = L(k/D_{\text{eff}})^{1/2}$ is the Thiele modulus.[39]

This solution has been used as the basis for obtaining a relationship between the observed and the true uptake coefficients, by equating the observed rate of species loss from the gas phase to the sum of the true loss to the external sample surface area A_{ext} plus the net diffusive flux into the sample.[10] Underwood et al.[30,31] adapted the KML approach to a Knudsen cell environment by implicitly setting the surface condition

$$A_o \frac{\gamma_o \bar{v}_g}{4} C_g = A_{\text{ext}} \frac{\gamma_t \bar{v}_g}{4} C_g - A_o D_{\text{eff}} \left.\frac{\partial C}{\partial x}\right|_0 \quad (6)$$

where the subscript g indicates values in the gas phase above the porous sample. With proper substitution of the concentration gradient, this equation can be rearranged to give

$$\gamma_o = \gamma_t \left[\frac{A_{\text{ext}}}{A_o} + \rho_b S_{\text{BET}} L \left(\frac{C_0 \bar{v}_p}{C_g \bar{v}_g}\right) \frac{\tanh(\phi)}{\phi}\right] \quad (7)$$

Taking $\bar{v}_g C_g = \bar{v}_p C_0$ and $A_{\text{ext}} = A_o L_s \rho_b S_{\text{BET}}$, where L_s is a surface roughness scale height, leads to the expression

$$\gamma_o = \gamma_t \rho_b S_{\text{BET}} \left[L_s + L \frac{\tanh(\phi)}{\phi}\right] \quad (8)$$

For slow reaction and fast diffusion, $k/D_{\text{eff}} \rightarrow 0$, $\tanh(\phi)/\phi \rightarrow 1$ and eq 1 is recovered with $A_t = A_o(L_s + L)\rho_b S_{\text{BET}} \approx A_o L \rho_b S_{\text{BET}}$; for fast reaction and slow diffusion, $k/D_{\text{eff}} \rightarrow \infty$, $\tanh(\phi)/\phi \rightarrow 0$ and eq 1 is recovered with $A_t \approx A_o L_s \rho_b S_{\text{BET}}$.

Evaluation of γ_t using eq 8 involves an iterative process, since γ_t also appears in the Thiele modulus. Numerical values are required for L, ρ_b, S_{BET}, T_p, L_s, and D_{eff}. The first four quantities are readily measured and L_s can be estimated from the characteristic particle diameter of the powder. In most practical cases, $L_s \ll L \tanh(\phi)/\phi$ and the precise numerical value of L_s is unimportant.

The dependence of γ_o on sample mass (through the relation $L = m/A_o\rho_b$) leads to two explicit expressions for γ_t. At small sample masses, γ_o is linearly dependent on mass and γ_t can be determined from experimental data via

$$\gamma_t = \frac{A_o}{S_{\text{BET}}} \left(\frac{d\gamma_o}{dm}\right) \quad (9)$$

so long as $\cosh^2(\phi)$ is $\sim$1. At large sample masses, γ_o is mass independent and γ_t can be determined from the asymptotic value $\bar{\gamma}_o$ using the expression

$$\gamma_t = \frac{\bar{v}\bar{\gamma}_o^{\,2}}{4 D_{\text{eff}} \rho_b S_{\text{BET}}} \quad (10)$$

so long as $L_s \ll (D_{\text{eff}}/k)^{1/2}$, which is typically the case. If the KML model is a correct representation of the physics at play, then both expressions should (nominally) reproduce the same value of γ_t from the experimental data. However, application of the full KML model or comparison of the two KML limits first requires knowledge of the effective diffusion coefficient in the porous medium.

4. Effective Diffusion Coefficients

The mathematical description of diffusive gas transport through porous media is adapted and generalized from analyses of gas diffusion through a single uniform, straight capillary tube. Gas diffusion in a capillary is governed by different physical process, depending on the dominance of molecule−molecule or molecule−surface collisions. These regimes are delineated using the Knudsen number, defined as the mean free path, λ, between molecule−molecule collisions divided by a characteristic dimension of the pore structure, $Kn = \lambda/r_p$. When $Kn \ll 1$, intermolecular collisions dominate transport and diffusion occurs in the continuum regime. When $Kn \gg 1$, molecule−surface collisions dominate transport and diffusion occurs in the free-molecular regime.

The general differential formulation of constant-pressure countercurrent diffusion of species A in a binary A−B mixture in a capillary tube is given by[40−42]

$$-\frac{P}{RT}\frac{d\chi_A}{dz} = \frac{\dot{J}_{AD}}{D_{AK}} + \frac{\dot{J}_{AD}\chi_B - \dot{J}_{BD}\chi_A}{D_{AB}} \quad (11)$$

where $\dot{J}_{AD}$ and $\dot{J}_{BD}$ are the diffusive mole fluxes in the positive z direction and χ_A and χ_B are the mole fractions of species A and B. D_{AB} is the conventional binary molecular diffusion coefficient, given to first-order approximation[43] by

$$D_{AB} = \frac{3k_B T}{8P\pi\sigma_{AB}^{\,2}\Omega_{AB}^{(1,1)*}}\sqrt{\frac{\pi k_B T}{2\mu_{AB}}} \quad (12)$$

where k_B is the Boltzmann constant. D_{AB} depends on the two gas species through the reduced mass, μ_{AB}, the collision diameter, σ_{AB}, and the collision integral for diffusion, $\Omega_{AB}^{(1,1)*}$. Equation 12 reveals an inverse dependence on total gas pressure P and a direct $\sim$3/2 power dependence on the gas temperature, T. (The collision integral is also weakly temperature dependent.)

D_{AK} is the Knudsen diffusion coefficient for species A given by

$$D_{AK} = \frac{2}{3} r_c \bar{v}_A \quad (13)$$

In the free-molecular regime, molecules diffuse independently of one another, unaffected by the total pressure or the gas composition. The form of eq 13 assumes a completely diffuse reflection of gas species colliding with surfaces. The mean molecular speed of gas A, given by $\bar{v}_A = (8RT/\pi M_A)^{1/2}$, introduces a square root dependence on temperature and an inverse square root dependence on molar mass. D_{AK} is also explicitly dependent on the capillary radius, r_c.

Equation 11 can be solved for the diffusive flux $\dot{J}_{AD}$ to give

$$\dot{J}_{AD} = -\frac{P}{RT}\frac{d\chi_A}{dz}\left[\frac{1}{D_{AK}} + \frac{1 - \alpha_A\chi_A}{D_{AB}}\right]^{-1} \quad (14)$$

with $\alpha_A = 1 + \dot{J}_B/\dot{J}_A$.

The bracketed term in eq 14 can be recognized as an effective diffusion coefficient for the *differential* form of Fick's First Law. For steady-state countercurrent diffusion in a constant-pressure open system, numerous researchers[40,41,44] have derived and experimentally confirmed the relationship $\dot{J}_B/\dot{J}_A = -(M_A/M_B)^{1/2}$ leading to $\alpha_A = 1 - (M_A/M_B)^{1/2}$.

Equation 14 may be integrated to obtain the effective diffusion coefficient for the *integrated* form of Fick's First Law

$$D_{\mathrm{Aeff}} = \frac{D_{\mathrm{AB}}}{\alpha_{\mathrm{A}}(\chi_{\mathrm{A0}} - \chi_{\mathrm{AL}})} \ln\left[\frac{1 - \alpha_{\mathrm{A}}\chi_{\mathrm{AL}} + \frac{D_{\mathrm{AB}}}{D_{\mathrm{AK}}}}{1 - \alpha_{\mathrm{A}}\chi_{\mathrm{A0}} + \frac{D_{\mathrm{AB}}}{D_{\mathrm{AK}}}}\right] \quad (15)$$

An analogous expression can be derived for species B; the binary molecular diffusion coefficient is symmetric ($D_{\mathrm{AB}} = D_{\mathrm{BA}}$) and the Knudsen diffusion coefficient is given by eq 13 with the appropriate substitution of molar mass.

The basic diffusion analysis for a capillary tube is retained for a porous media but with the diffusion coefficients D_{AB} and D_{AK} replaced by $(\epsilon/\tau)D_{\mathrm{AB}}$ and $(\epsilon/\tau)D_{\mathrm{AK}}$, where (ϵ/τ) is the ratio of porosity divided by tortuosity. Tortuosity is defined as the average (convoluted) distance traveled by the diffusive flow, divided by the equivalent linear distance along the macroscopic concentration gradient. In practice, the tortuosity is an empirical constant with characteristic values ranging from 1 to 8, for a variety of granular porous materials.[45] The application of eq 13 to a porous media also requires replacement of the capillary radius r_{c} by a characteristic pore dimension r_{p}.

Flow tubes, diffusion tubes, and Knudsen cell reactors are typically operated at low total pressures, and the pore dimensions in ice films and mineral powder beds used for heterogeneous atmospheric chemistry experiments are typically on the micrometer level. Therefore, gas diffusion within these porous media is expected to lie in the free-molecular regime.

The KML model, as presented by Keyser et al.[34,38] for application to vapor-deposited ice films, is explicitly formulated for the Knudsen diffusion regime by incorporating the substitution $D_{\mathrm{eff}} = 2\epsilon r_{\mathrm{p}}\bar{v}/3\tau$, where r_{p} is taken as twice the ratio of pore volume to pore surface area. Further approximation of the porous media as a collection of uniform spherical particles with diameter d provides the additional relation $S_{\mathrm{BET}} = 6/\rho_{\mathrm{t}}d$, leading finally to an explicit expression for the Theile modulus of

$$\phi = \frac{L}{d}\frac{3\rho_{\mathrm{b}}}{2(\rho_{\mathrm{t}} - \rho_{\mathrm{b}})}\sqrt{3\tau\gamma_{\mathrm{t}}} \quad (16)$$

which has been used by all subsequent investigators.

5. Countercurrent Diffusion Measurement Theory

Effective diffusion coefficients were measured using a constant-pressure countercurrent diffusion method.[41,46] In this method, a porous sample is suspended between flows of two different gas species, A and B, as shown schematically in Figure 3.

As the two gas streams flow past the sample, each species diffuses down its respective concentration gradient through the sample into the other gas. Experiments are performed under steady-state conditions with inert gases. Conservation of molecules dictates the relationships

$$\dot{N}_{\mathrm{AD}} = \frac{(\chi_{\mathrm{A}}/\chi_{\mathrm{B}})_2[\dot{N}_{\mathrm{B}}(\chi_{\mathrm{A}}/\chi_{\mathrm{B}})_1 - \dot{N}_{\mathrm{A}}]}{(\chi_{\mathrm{A}}/\chi_{\mathrm{B}})_1 - (\chi_{\mathrm{A}}/\chi_{\mathrm{B}})_2} \quad (17a)$$

$$\dot{N}_{\mathrm{BD}} = \frac{\dot{N}_{\mathrm{A}} - \dot{N}_{\mathrm{B}}(\chi_{\mathrm{A}}/\chi_{\mathrm{B}})_2}{(\chi_{\mathrm{A}}/\chi_{\mathrm{B}})_1 - (\chi_{\mathrm{A}}/\chi_{\mathrm{B}})_2} \quad (17b)$$

where $\dot{N}_{\mathrm{AD}}$ and $\dot{N}_{\mathrm{BD}}$ are the diffusive molecular flows through the porous sample. $\dot{N}_{\mathrm{A}}$ and $\dot{N}_{\mathrm{B}}$ are the convective molecular flows of each species introduced upstream of the sample and χ_{A} and χ_{B} are the mole fractions of each species in the gas mixture downstream of the sample. These expressions allow

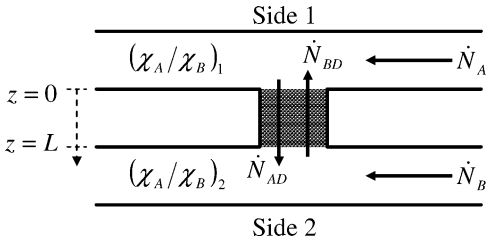

Figure 3. Schematic diagram of countercurrent diffusion experiment.

for experimental determination of diffusive flows from measurements of the upstream gas flow and the downstream gas composition on each side of the porous sample.

The diffusive flows can also be expressed in terms of effective diffusion coefficients and concentration gradients across the sample using the integrated form of Fick's First Law. We take $z = 0$ on side 1 of the sample and $z = L$ on side 2 of the sample. For a cylindrical sample of radius r, this gives

$$\dot{N}_{\mathrm{AD}} = \dot{J}_{\mathrm{AD}}\pi r^2 = -D_{\mathrm{A,eff}}\frac{P\pi r^2}{RTL}(\chi_{\mathrm{AL}} - \chi_{\mathrm{A0}}) \quad (18a)$$

$$\dot{N}_{\mathrm{BD}} = -\dot{J}_{\mathrm{BD}}\pi r^2 = D_{\mathrm{B,eff}}\frac{P\pi r^2}{RTL}(\chi_{\mathrm{BL}} - \chi_{\mathrm{B0}}) \quad (18b)$$

By equating eqs 17a and 18a and 17b and 18b, the following expressions are obtained for the effective diffusion coefficients

$$D_{\mathrm{A,eff}} = \frac{LRT}{\pi r^2 P}\frac{(\chi_{\mathrm{A}}/\chi_{\mathrm{B}})_2[\dot{N}_{\mathrm{B}}(\chi_{\mathrm{A}}/\chi_{\mathrm{B}})_1 - \dot{N}_{\mathrm{A}}]}{(\chi_{\mathrm{A0}} - \chi_{\mathrm{AL}})[(\chi_{\mathrm{A}}/\chi_{\mathrm{B}})_1 - (\chi_{\mathrm{A}}/\chi_{\mathrm{B}})_2]} \quad (19a)$$

$$D_{\mathrm{B,eff}} = \frac{LRT}{\pi r^2 P}\frac{\dot{N}_{\mathrm{A}} - \dot{N}_{\mathrm{B}}(\chi_{\mathrm{A}}/\chi_{\mathrm{B}})_2}{(\chi_{\mathrm{BL}} - \chi_{\mathrm{B0}})[(\chi_{\mathrm{A}}/\chi_{\mathrm{B}})_1 - (\chi_{\mathrm{A}}/\chi_{\mathrm{B}})_2]} \quad (19b)$$

Some ambiguity is inherent in specifying mole fractions at the sample boundaries. Many researchers have taken $\chi_{\mathrm{A0}} = \chi_{\mathrm{BL}} = 1$ and $\chi_{\mathrm{AL}} = \chi_{\mathrm{B0}} = 0$, invoking the presumption that fast gas flows over the sample surfaces continuously sweep away the diffusing component. However, one may equally well use the measured downstream gas compositions on sides 1 and 2 as the boundary conditions; that is, $\chi_{\mathrm{A0}} = \chi_{\mathrm{A1}}$, $\chi_{\mathrm{AL}} = \chi_{\mathrm{A2}}$, $\chi_{\mathrm{B0}} = \chi_{\mathrm{B2}}$, and $\chi_{\mathrm{BL}} = \chi_{\mathrm{B1}}$. Because the convective gas flows are much larger than the diffusive mass flows in our experiments, the numerical difference between these two choices is slight, amounting to a few percent at most. We use the latter implementation in our data analysis.

The critical gas composition measurements involve determination of the minor gas component on each side of the sample, χ_{A2} and χ_{B1}. After inserting our choice of boundary conditions, eqs 19a and 19b can be further sharpened by eliminating the mole fractions of the major components using the identities $\chi_{\mathrm{A1}} = 1 - \chi_{\mathrm{B1}}$ and $\chi_{\mathrm{B2}} = 1 - \chi_{\mathrm{A2}}$. The final expressions for the effective diffusion coefficients in terms of known or measured parameters are

$$D_{\mathrm{A,eff}} = \frac{LRT}{\pi r^2 P}\frac{\chi_{\mathrm{A2}}[\dot{N}_{\mathrm{B}} - \chi_{\mathrm{B1}}(\dot{N}_{\mathrm{A}} + \dot{N}_{\mathrm{B}})]}{(1 - \chi_{\mathrm{A2}} - \chi_{\mathrm{B1}})^2} \quad (20a)$$

$$D_{\mathrm{B,eff}} = \frac{LRT}{\pi r^2 P}\frac{\chi_{\mathrm{B1}}[\dot{N}_{\mathrm{A}} - \chi_{\mathrm{A2}}(\dot{N}_{\mathrm{A}} + \dot{N}_{\mathrm{B}})]}{(1 - \chi_{\mathrm{A2}} - \chi_{\mathrm{B1}})^2} \quad (20b)$$

We measure diffusion coefficients at sufficiently low pressures that eq 15 returns $D_{\mathrm{Aeff}} = (\epsilon/\tau)D_{\mathrm{AK}}$. We use the analyses above

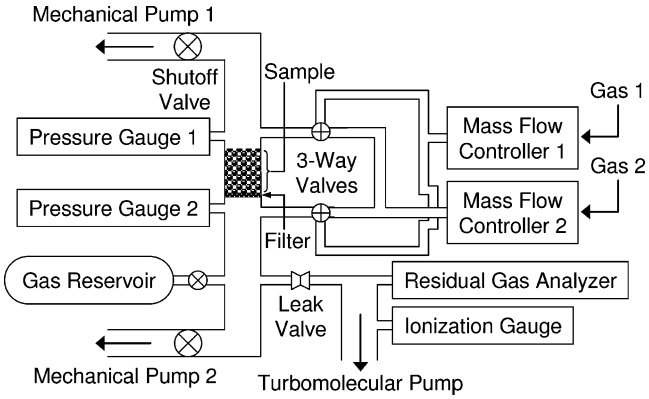

Figure 4. Schematic diagram of experimental setup.

to set our operating conditions, check the consistency of our experimental measurements, and connect our diffusion coefficient measurements to characteristic descriptors of the porous media.

6. Experimental Apparatus and Test Procedures

Countercurrent Diffusion. A diagram of the experimental apparatus is shown in Figure 4. The powder bed is contained in a 2.20 cm diameter stainless steel tube, supported on a thin woven Teflon membrane filter with 1.0 μm pores (Pall Life Sciences TF-1000). A known mass of powder is placed on the filter and compacted by hand using a slip-fit Teflon rod. The height of the compacted bed is determined from the difference in the lengths of the Teflon rod protruding from the stainless steel tube with or without the powder in place. Lengths are measured with a venier micrometer. Bed heights have maximum uncertainties of $\sim$0.02 cm and are used to determine the bulk density of the powder bed.

The gas flows streaming over the sample on side 1 (the upper flow path) and side 2 (the lower flow path) are regulated with electronic mass flow controllers (50 sccm Tylan series 2900). The counter-diffusing gases—generally argon and helium—were chosen to be chemically inert and have a large difference in atomic mass. All gases (Air Products 99.99+%) are used from the cylinders without further purification. The two gas flows are removed by independent vacuum lines to eliminate downstream mixing and the potential for back-diffusion.

Gas pressures on both sides of the porous sample bed are measured using 1 Torr capacitance manometers (Baratron models 310 and 220). For some experiments, a 1 Torr differential manometer (Baratron model 144) is used to maintain a negligible pressure gradient across the sample. Uniform pressures are set by adjusting the mass flow rates of the two incoming gas streams. In all cases, the pressure difference across the porous sample is maintained at less than 1 mTorr to mitigate any possibility of pressure-driven gas transport.

The mass flow controllers are periodically intercalibrated by placing them in series and the full-scale pressure readings of the 1 Torr manometers are periodically compared to account for any systematic pressure differences among gauges. Pressure measurement and mass flow measurement errors do not exceed 1%.

The gas composition is measured using a quadrupole mass spectrometer (SRS RGA200) that samples the lower flow path through an adjustable precision leak valve (Varian). The pressure at the mass spectrometer is maintained on the order of 10^{-6} Torr by means of a Blazers turbomolecular pump; this pressure is verified using an ionization gauge. Mass spectrometer signals are collected on a personal computer running software manufactured by Stanford Research Systems. Gas composition measurements are made in "selected ion" mode, in which the quadrupole repeatedly scans across only the peaks of interest to determine their concentration. For improved measurement precision, only the diffusing gas (trace gas) mixing ratio is calculated; the remainder of the gas flow is assumed to consist of the nondiffusing species. Ions are detected using a Faraday cup rather than with an electron multiplier, so the mass spectrometer signal is invariant with ion mass. For each diffusion measurement, approximately 30 scans are averaged to determine the mixing ratio.

In our setup, the gas mixture is only sampled on the lower side of the powder bed; however, the gas composition on both sides is needed to determine the diffusive fluxes. To achieve this, the mixing ratios of the minor species downstream of the porous sample are determined sequentially. First, gas A is introduced into the upper flow path and gas B into the lower flow path. The diffusion of A through the porous sample into B is observed by measuring the mixing ratio of A in the lower flow path. Then, the gases are interchanged at the diffusion apparatus inlets using two 3-way valves and the mixing ratio of gas B is measured in the lower flow path.

Sampling through a leak valve introduces the possibility that the gas composition measured in the low-pressure mass spectrometer region differs from that in the higher pressure flow. For an ideal orifice, the effusive sampling rate for different gases would be inversely proportional to $(M)^{1/2}$, but this relationship cannot be assumed to hold precisely for a leak valve operated at different settings and upstream pressures. Moreover, the gas composition within the mass spectrometer chamber may also be affected by the relative pumping efficiencies of the turbomolecular pump for different gases.

To account for possible sampling biases, the following procedure is used. First, the linearity of the mass spectroscopic detection is confirmed over the full mixing ratio range of 0 to 100% at various total pressures. Gas mixtures were set by dynamic dilution, mixing two pure flowing gas streams regulated by independent mass flow controllers, before introduction into the diffusion apparatus. To obtain greater resolution at small mixing ratios—mixing ratios of the order 1% must typically be determined in the diffusion experiments—further calibrations are performed by replacing, in turn, each of the pure gas streams with a source containing a premixed 5.00% dilution. In this way, signal linearity at small mixing ratios is also confirmed.

Before every diffusion experiment, each pure gas is first simultaneously introduced to both upper and lower flow paths, to determine the mass spectrometer readings at zero and unity mixing ratios. These readings are then used to scale the measurements of the minor constituents during the diffusion experiment. The validity of this approach can be checked experimentally, by confirming the expected $\dot{N}_{He,D}/\dot{N}_{Ar,D} = (10)^{1/2}$ for He and Ar test gases. Since uncertainties in the convective gas flows are very small, deviations from this relationship largely reflect uncertainties in the minor constituent mole fractions.

Transient Pressure Decay. As a redundant measurement, we also determine the effective diffusion coefficients of our powder beds using an alternate transient pressure decay method, wherein a known gas volume is exhausted through the porous sample while the pressures upstream and downstream of the sample are measured as a function of time. In the free-molecular regime, where intermolecular collisions are negligible, this transient pressure decay technique should produce effective Knudsen diffusion coefficients equivalent to those measured by the countercurrent diffusion method.

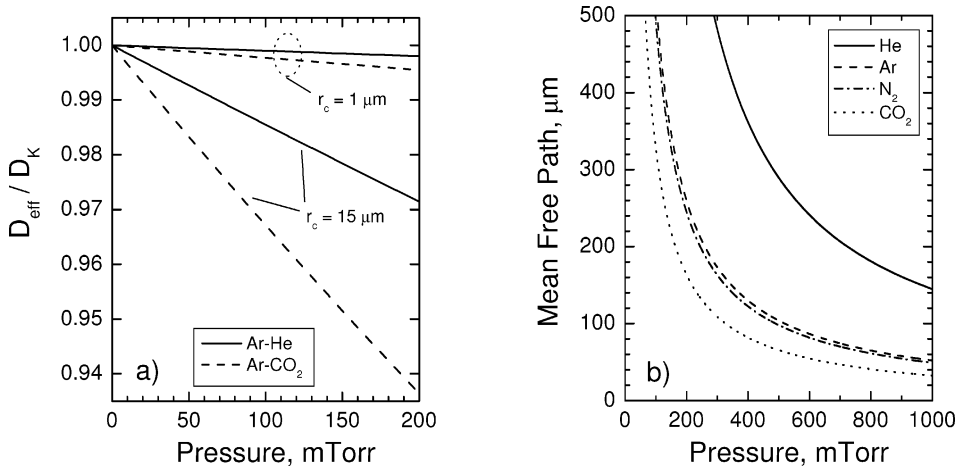

Figure 5. Calculated 295 K pressure dependence of (a) the ratio of effective to Knudsen diffusion coefficients for a capillary tube and (b) the mean free path.

In the transient measurements, a valve to a gas reservoir below the sample is opened, significantly increasing the lower chamber volume. The chambers on both sides of the sample are filled to a static pressure of 1 Torr. Then, the valve to the upper mechanical pump is opened, quickly evacuating the upper chamber to less than 50 mTorr. The changing pressures are measured with 1 Torr Baratron capacitance manometers, whose analog outputs are digitized at ~1 Hz, using an SRS245 analog to digital interface, transferred across a GPIB interface, and acquired on a PC using a custom-programmed LabView application. Independent measurements are conducted using both nitrogen and helium as the exhausting gas.

The transient pressure decay in the lower chamber is described by

$$\frac{dP_l}{dt} = \frac{-1}{\tau_p}[P_l(t) - P_u(t)] \tag{21}$$

with the characteristic time constant

$$\tau_p = \frac{VL}{D_{eff}\pi r^2} \tag{22}$$

The subscripts u and l indicate the upper and lower chambers, t is time, and V is the volume of the lower chamber. If P_u is zero, eq 21 can be integrated to give an exponential of P_l in time and the characteristic time constant can be determined from an exponential fit to the experimental P_l decay curve.

Because of pumping speed limitations, the pressure in the upper chamber does not drop instantaneously but changes during the initial stages as the lower chamber is exhausted. A more complete description of the time constant is obtained from

$$\tau_p = \frac{\int_0^t [P_l(t)1 - P_u(t)]\,dt}{[P_l(0)1 - P_l(t)]} \tag{23}$$

For several experiments, signals from the two manometers were subtracted and then integrated numerically to evaluate eq 23. Comparison of the time constants obtained in these two ways revealed insignificant differences, indicating that pressure transients in the upper chamber did not bias the extracted time constants.

Test Conditions. To ensure that operating conditions during countercurrent diffusion experiments lie in the free-molecular regime, we have evaluated the ratio D_{eff}/D_K using eqs 13 and 15 for a single capillary tube as a function of pressure for Ar−He and Ar−CO_2 mixtures at 295 K; see Figure 5a. For bimolecular diffusion coefficients, we have used the expressions $D_{Ar-He} = 558.125/P$ and $D_{Ar-CO_2} = 113.637/P$, where diffusion coefficients are in $cm^2\ s^{-1}$ and pressures in Torr.[47] For a characteristic pore dimension of 1 μm, approximately the largest value calculated for our powder specimens (see Table 1), D_{eff}/D_K deviates by less than 0.5% from unity over a pressure range from 0 to 200 mTorr for both gas mixtures. Even when the characteristic pore dimension is increased to 15 μm, D_{eff}/D_K remains within 3% of unity for the Ar−He mixture. Therefore, we conduct our countercurrent diffusion experiments at fixed pressures of 50, 100, and 200 mTorr using Ar and He. Additional measurements using Ar and CO_2 were performed only for γ-Fe_2O_3 which has the smallest computed pore dimension of ~0.1 μm.

Figure 5b shows the pressure dependence of the mean free path for He, Ar, N_2, and CO_2 at 295 K in the 0 to 1 Torr range. The mean free path in micrometers was calculated from the expression[48] $687.65/P\sigma^2$ where pressure is in Torr and the collision cross-section[49] σ is in angstroms. The mean free paths of all gases exceed 100 μm below 200 mTorr; therefore, the Knudsen number also exceeds 100 for a 1 μm characteristic pore size below 200 mTorr. At the higher pressures used in the transient pressure decay measurements and with a characteristic pore size of 15 μm, the smallest Knudsen numbers are 9.6 and 3.3 for He and N_2 at 1 Torr.

7. Experimental Results

Capillary Array. As a check, an initial set of experiments is performed on a capillary array to compare our two measurement approaches. The capillary array is manufactured of lead glass by Burle Industries (GCA 09/32/25/0/20LM). It is specified to contain parallel 27.07 μm diameter capillaries (with less than 1% variation within the array) at a center-to-center spacing of 35.09 μm, resulting in faces with 54% open surface area. The 2.0 mm thick capillary array is sealed in a sample holder between thin rubber gaskets that leave a porous region of 4.0 mm radius available for diffusion. The sample holder is then held in the sample compartment with a tightly sealed O-ring. The length-to-radius ratio of each capillary is approximately 148, sufficient for fully developed gas flow inside the capillary, as evidenced by a negligible Clausing correction factor of 0.02.[48]

Geometrically, a capillary array is the best-characterized porous sample available and diffusion through a capillary should

TABLE 2: Experimental Results for the Capillary Array

countercurrent diffusion					transient pressure decay		
P mTorr	$\dot{N}_{He,D}/\dot{N}_{Ar,D}$	$D_{Ar,eff}$ cm^2 s^{-1}	$D_{He,eff}$ cm^2 s^{-1}	$D_{M,eff}/\bar{v}_M$ μm	gas	$D_{M,eff}$ cm^2 s^{-1}	$D_{M,eff}/\bar{v}_M$ μm
50	2.34	13.2	30.9	2.91	He	35.8	2.87
50	2.31	12.2	28.2	2.68	He	32.8	2.63
100	3.08	12.0	36.9	2.99	He	47.4	3.79
100	3.11	12.6	39.0	3.15	He	39.1	3.13
100	2.97	12.7	37.6	3.11	He	39.2	3.13
100	2.93	12.8	37.5	3.12		**39 ± 11**	
100	2.91	12.4	35.9	3.00	N_2	18.2	3.85
200	3.17	11.2	35.5	2.84	N_2	18.1	3.83
	3.0 ± 0.3	**12 ± 1**	**35 ± 7**	**2.9 ± 0.6**		**18 ± 1**	**3.3 ± 1.0**

be reasonably well described by the formulas presented above. However, in an array, each capillary opening is in very close proximity to its neighbors and does not emerge isolated on an infinite solid plane surface, the usual idealization employed in gas kinetic theory analyses of transport and entrance effects in capillaries. On the basis of eq 13 and $\epsilon/\tau = 0.54/1$, the effective room-temperature Knudsen diffusion coefficients for helium, argon, and nitrogen in the capillary array are $D_{He,eff} = 60.7$ cm^2 s^{-1}, $D_{Ar,eff} = 19.2$ cm^2 s^{-1}, and $D_{N_2,eff} = 23.0$ cm^2 s^{-1}, respectively. These values should be viewed as upper limits, since any obstructions present inside the capillaries (e.g., dust), as well as unaccounted for end effects, will decrease the experimental diffusive flux and hence the measured effective diffusion coefficients.

Table 2 shows the results of the capillary array measurements. The maximum experimental uncertainty of individual measurements is approximately 10% for the flux ratios and 5% for the diffusion coefficients. Mass flow, pressure, and geometric measurement uncertainty is small (~1%); the major error contributions are associated with extracting mole fractions from mass spectrometer data and time constants from pressure transients. Averaged quantities with expanded 2-σ uncertainties are shown in Table 2 in bold type.

The countercurrent diffusion experiments return values of $D_{Ar,eff} = 12 \pm 1$ cm^2 s^{-1} and $D_{He,eff} = 35 \pm 7$ cm^2 s^{-1}, roughly 40% lower than the theoretical values. The transient pressure decay measurements give $D_{He,eff} = 39 \pm 11$ cm^2 s^{-1} and $D_{N_2,eff} = 18 \pm 1$ cm^2 s^{-1}, again lower than the theoretical values, though by only about 20% in the case of nitrogen. There is good agreement between the effective helium diffusion coefficients obtained by the two different techniques.

Within experimental scatter, the countercurrent diffusion measurements show no systematic variations with pressure, consistent with the expectation that diffusion occurs within the free-molecular regime. The average experimental $\dot{N}_{He,eff}/\dot{N}_{Ar,eff}$ ratio is ~6% below the theoretical $(10)^{1/2} \cong 3.16$ value. The largest deviations from theoretical values appear in the 50 mTorr data, which is not unexpected as the 50 mTorr data are obtained near the low-pressure limit of our experimental approach. All of the 100 and 200 mTorr data lie within 12% of the theoretical value, a level of agreement comparable to that observed by Remick and Geankoplis[42] in their study of binary He−N_2 countercurrent diffusion in capillaries. If the transient pressure decay measurements are also performed in the free-molecular regime, then the ratio $D_{He,eff}/D_{N_2,eff}$ should equal $(7)^{1/2} \cong 2.65$; experimentally, we find a lower value of 2.15, which may indicate some contribution of pressure-driven flow at the higher pressures at the start of the decay curves. Any such contribution should become negligible for the powder bed measurements where the Knudsen numbers increase by an order of magnitude.

Because Knudsen diffusion coefficients depend on the ratio $(T/M)^{1/2}$ through the thermal velocity, measured values differ for each test gas and temperature. An experimental quantity more representative of the porous medium is obtained by normalizing individual diffusion coefficient measurements by the thermal velocity of the test gas and then averaging these values. This normalized diffusion coefficient has dimensions of length and contains only geometric descriptors of the porous medium, since by definition in the free-molecular regime, $D_{M,eff}/\bar{v}_M = 2\epsilon r_p/3\tau$. The fifth and eighth columns in Table 2 list this quantity for the two measurement approaches. The theoretical value of $D_{M,eff}/\bar{v}_M$ for the capillary array is 4.87 μm. The average values obtained from the countercurrent diffusion and transient pressure decay measurements are 2.9 ± 0.6 and 3.3 ± 1.0 μm, values that agree within in their respective uncertainties and which are ~30−40% smaller than the theoretical value. We consider this level of agreement between the results of two measurement techniques acceptable and sufficient for our purposes.

Oxide Powders. Effective diffusion coefficients for packed powder beds were measured by the countercurrent diffusion technique at pressures of 50, 100, and 200 mTorr and at various powder bed depths ranging from about 0.5 to 2.8 cm. The counter diffusing gases were always argon and helium, with the exception of three experiments conducted on γ-Fe_2O_3 using argon and carbon dioxide. In all, 26 experiments were run on the four different materials. Each experiment yielded two effective diffusion coefficients, one for argon and one for helium (or carbon dioxide). The two gas-dependent diffusion coefficients were then normalized by their thermal speeds and averaged to produce a single $D_{M,eff}/\bar{v}_M$ value per experiment.

Table 3 summarizes the experimental parameters of each test (bed depth and pressure), along with the experimental values of the diffusive flux ratio, the effective argon, helium and carbon dioxide diffusion coefficients, and the normalized effective diffusion. Again, averaged quantities are listed in bold face type with conservative 2-σ uncertainties.

The experimental flux ratios are uniformly lower than the theoretical flux ratios $\dot{N}_{He,D}/\dot{N}_{Ar,D} \cong 3.16$ and $\dot{N}_{CO_2,D}/\dot{N}_{Ar,D} \cong 1.05$. This suggests an unidentified bias error residing in the mass spectroscopic calibrations, which seems most pronounced in the 50 mTorr data. Nevertheless, the average experimental flux ratios are all within 20% of the theoretical values; furthermore, the theoretical values lie within the 2-σ error bars assigned to the experimental averages. This level of agreement between theory and experiment is similar to that reported by Masamune and Smith,[50] Wakao and Smith,[51] Rothfeld,[52] and Henry et al.,[46] for countercurrent diffusion experiments on a variety of porous ceramics and catalysts.

Multiple diffusion coefficient measurements under constant experimental conditions are very reproducible; for example, the standard deviations of the P =100 mTorr data of the three α-Al_2O_3 $L = 0.95$ cm replicates is ~2%, of the three α-Fe_2O_3 $L = 0.51$ cm replicates is ~3%, and the five Mg_2SiO_4 $L =$

TABLE 3: Countercurrent Diffusion Measurement Results for Oxide Powders

L cm	P mTorr	$\dot{N}_{He,D}/\dot{N}_{Ar,D}$	$D_{Ar,eff}$ cm^2 s^{-1}	$D_{He,eff}$ cm^2 s^{-1}	$D_{M,eff}/\bar{v}_M$ μm
			Mg_2SiO_4		
2.15	50	2.28	1.53	3.50	0.334
2.15	100	3.00	1.50	4.50	0.370
2.15	100	2.95	1.43	4.22	0.350
2.15	100	3.16	1.35	4.25	0.340
2.15	100	2.79	1.40	3.90	0.333
2.15	200	3.16	1.27	4.02	0.322
		2.9 ± 0.6	**1.4 ± 0.2**	**4.1 ± 0.6**	**0.34 ± 0.04**
			α-Al_2O_3		
0.95	100	2.76	0.598	1.65	0.142
0.95	100	2.61	0.642	1.68	0.148
0.95	100	2.73	0.606	1.65	0.143
1.43	50	2.22	0.895	1.99	0.193
1.43	100	2.97	0.792	2.34	0.194
1.43	200	3.15	0.734	2.31	0.185
1.78	100	2.81	0.550	1.54	0.131
2.80	100	2.60	0.775	2.01	0.178
		2.7 ± 0.6	**0.70 ± 0.24**	**1.9 ± 0.6**	**0.16 ± 0.06**
			α-Fe_2O_3		
0.51	100	2.81	0.952	2.67	0.227
0.51	100	2.89	0.905	2.62	0.219
0.51	100	2.95	0.879	2.60	0.215
1.31	50	2.74	1.30	3.58	0.308
1.31	100	3.08	1.16	3.57	0.290
1.31	200	3.16	1.09	3.44	0.276
		2.9 ± 0.4	**1.0 ± 0.4**	**3.1 ± 1.0**	**0.26 ± 0.08**
			γ-Fe_2O_3		
1.98	50	2.00	1.17	2.34	0.241
1.98	100	2.62	1.17	3.06	0.271
1.98	200	3.01	1.11	3.34	0.274
		2.5 ± 1.0		**2.9 ± 1.0**	
1.98	50	0.834 [a]	1.02	0.852 [a]	0.241
1.98	50	0.797 [a]	1.07	0.847 [a]	0.248
1.98	200	1.02 [a]	1.15	1.17 [a]	0.300
		0.88 ± 0.24 [a]	**1.1 ± 0.2**	**0.95 ± 0.36**[a]	**0.26 ± 0.04**

[a] Experiments with CO_2 and Ar.

TABLE 4: Transient Pressure Drop Measurement Results for Oxide Powders

	Mg_2SiO_4	α-Al_2O_3	α-Fe_2O_3	γ-Fe_2O_3
L, cm	1.69	1.37	1.66	1.93
$D_{N_2,eff}$, cm^2 s^{-1}	0.931	0.771	1.31	1.71
$D_{He,eff}$, cm^2 s^{-1}	2.40	2.07	3.50	4.31
$D_{He,eff}/D_{N_2,eff}$	2.58	2.68	2.67	2.52
$D_{M,eff}/\bar{v}_M$, μm	0.20	0.16	0.28	0.35

2.15 cm replicates is ~5%. Slightly larger variability is found when the pressures are changed at a fixed bed depth. Little difference is seen when a different gas combination is used for the same powder bed and pressure (CO_2−Ar instead of He−Ar for γ-Fe_2O_3). The largest variability is clearly introduced when different powder beds of the same material are tested. Since no systematic dependence on bed depth is observed (see the α-Al_2O_3 data), we attribute this variability to differences in powder packing. So, for example, the 2-σ uncertainties on the average values for Mg_2SiO_4 and γ-Fe_2O_3 are 12% and 15%, but those of α-Fe_2O_3 and α-Al_2O_3 are 31% and 38%.

Table 4 shows the results of the transient pressure drop technique applied to the powder samples. Only one measurement is available for each gas−material combination, so statistical errors are not reported. Known measurement uncertainties (in bed depth, pressure measurement, and curve fitting) combine to produce no more than a 10% uncertainty in the extracted effective helium and nitrogen diffusion coefficients, but scatter associated with multiple determinations would undoubtedly increase this further. The experimental ratio of diffusion coefficients $D_{He,eff}/D_{N_2,eff}$ lies within 5% of the theoretical $(7)^{1/2} \cong 2.65$ value for each material, consistent with the free-molecular diffusion regime and the absence of pressure driven flow contributions.

TABLE 5: Diffusion Parameter Calculations

	$(D_{M,eff}/\bar{v}_M)_{theo}$, μm		τ_{fit}	
	$\tau = 1$	$\tau = 5$	countercurrent	transient
Mg_2SiO_4	0.35	0.069	1.02	1.73
α-Al_2O_3	0.16	0.032	1.01	1.01
α-Fe_2O_3	0.15	0.030	0.57	0.83
γ-Fe_2O_3	0.061	0.012	0.24	0.17

The ratios $(D_{M,eff}/\bar{v}_M)_{transient}/(D_{M,eff}/\bar{v}_M)_{countercurrent}$ for Mg_2SiO_4, α-Al_2O_3, α-Fe_2O_3, and γ-Fe_2O_3 are, respectively, 0.59, 1.00, 1.08, and 1.35, with associated uncertainties of about 30−50%. Excellent agreement between the two techniques is found for α-Al_2O_3 and α-Fe_2O_3; less so for Mg_2SiO_4 and γ-Fe_2O_3 where the discrepancies reach 40%.

8. Discussion

How close are the measured diffusion coefficients to estimates based on powder bed characteristics? From eq 13, $D_{M,eff}/\bar{v}_M = 2\epsilon r_p/3\tau$. The porosity of a powder bed can be determined within a few percent from dimension and mass measurements, but unique numerical values for τ and r_p are not readily available, since both quantities depend in complicated ways on the pore structure and bed geometry.

The first two columns of Table 5 give the values of $(D_{M,eff}/\bar{v}_M)_{theo}$ computed using the approximations $r_p = 2\epsilon/\rho_b S_{BET}$ and $\tau = 1$ or 5. The third and fourth columns list values of tortuosity that will reproduce the experimental $D_{M,eff}/\bar{v}_M$ values measured by the countercurrent diffusion or transient pressure decay techniques. In general, the results are consistent with the ideas that powder bed tortuosity is low and the characteristic pore dimension is underestimated.

Computations with $\tau = 5$ significantly underpredict the experimental $D_{M,eff}/\bar{v}_M$ values for all powder beds, by factors ranging from 4 to 20. Though $\tau = 1$ is unrealistically low for a real powder bed, the experimental countercurrent diffusion measurements for both Mg_2SiO_4 and α-Al_2O_3 are closely matched by $(D_{M,eff}/\bar{v}_M)_{theo}$, as are the transient pressure decay results for α-Al_2O_3. For Mg_2SiO_4, the transient pressure decay results can be reproduced by increasing the tortuosity slightly to 1.73. The values of $(D_{M,eff}/\bar{v}_M)_{theo}$ for the α-Fe_2O_3 and γ-Fe_2O_3 powders still underpredict the experimental values by a large margin when $\tau = 1$ is used. To reproduce the experimental results for the Fe_2O_3 powders, nonphysical adjustments of the tortuosities to values below 1 are required.

While we do not subscribe to this view, one could interpret the capillary array measurements to suggest that our experimental techniques systematically return diffusion coefficient values about 30% lower than the true values. However, correcting for such an effect would decreases τ_{fit} even further.

These results indicate that $r_p = 2\epsilon/\rho_b S_{BET}$ tends to underestimate the characteristic pore size of the powder beds, most significantly for the two Fe_2O_3 materials, but probably also to a lesser extent for Mg_2SiO_4 and α-Al_2O_3. A possible explanation for this finding is that in these highly porous powder beds net diffusive transport may be dominated by the collection of paths that link the largest pore spaces together (i.e., the paths of least resistance). However, the BET surface area measurement samples the *total* surface area, not just of the largest channels, so r_p would be underestimated. This effect would be greatest for powders with very small particles where agglomeration from

interparticle electrostatic forces can lead to local volumes of high packing density separated by large pore spaces, consistent with our finding the lowest extracted tortuosities for the iron oxide powder beds. The approximation $r_p = 2\epsilon/\rho_b S_{BET}$ allows calculation from easily measured quantities but is not a unique definition and includes no structure information. Unfortunately, there are no universally accepted or easily applied alternatives.

Powder bed porosity is known to increase rapidly with decreasing particle size over the range 0.1 to 10 μm, regardless of particle shape, as interparticle electrostatic forces overwhelm the force exerted by gravity and prevent efficient packing.[53] Both the measured particle size distributions and the SEM pictures show that the α-Al_2O_3, α-Fe_2O_3, and γ-Fe_2O_3 particles fall in this range and the high powder bed porosities reflect the resulting inefficient packing. Higher porosity, in turn correlates with lower tortuosities and larger characteristic pore dimensions.

A variety of empirical and theoretical correlations have been proposed in the literature relating tortuosity to porosity. All begin at $\tau = 1$ when $\epsilon = 1$ and predict increasing tortuosity with decreasing porosity.[54] Monte Carlo simulations of Knudsen diffusion in sphere beds with various diameter distributions and geometric arrangements,[55,56] as well as in random binary media[57] and random overlapping fiber beds,[58] show similar trends. However, both experiment and simulation suggest that, for powder beds with $\epsilon \geq 0.5$, tortuosities exceeding 5 are highly unlikely.[55] Note that most powder beds used in heterogeneous atmospheric chemistry experiments have porosities exceeding 0.5.[26,28,30,31,59,60]

A series of experimental Knudsen diffusion measurements in pressed-pellets of submicrometer silica spheres[61−63] ($\epsilon = \sim 0.3-0.4$) returned values scattered about $\tau = 1.5$ for a variety of characteristic pore size definitions, including $r_p = 2\epsilon/\rho_b S_{BET}$. Tomadakis and Sotirchos[58] observed that with this approximation for r_p their Monte Carlo simulations of Knudsen diffusion in random overlapping fiber beds returned values of tortuosity smaller than 3 for all beds with porosities exceeding 0.45. Experiments by Wang and Smith on catalyst pellets with porosities of 0.57 and 0.68 demonstrated that using $r_p = 2\epsilon/\rho_b S_{BET}$ can result in apparent tortuosities extracted from Knudsen diffusion coefficients that fall below 1 (as seen in Table 5 for the Fe_2O_3 powder beds).[64]

In summary, our measured effective diffusion coefficient values seem reasonable and are consistent with past experiments and numerical simulations for highly porous media where low tortuosities are expected, especially when the approximation $r_p = 2\epsilon/\rho_b S_{BET}$ is employed.

9. Ramifications

What are the ramifications of our experiments for extracting "true" uptake coefficients from observed values using the KML model? First, it is evident that Knudsen diffusion coefficients estimated from powder bed characteristics can have large uncertainties, so direct correction of individual data points using estimated diffusion coefficients in the KML model will also generate large uncertainties. These uncertainties arise from the need to select values for r_p and τ. If the Thiele modulus is further expressed using a monodiameter spherical particle approximation as in eq 16, additional uncertainty is introduced if the equivalent sphere diameter is assigned a value from independent measurements, for example, those estimated from SEM images or sieving,[27,28,59] rather than from the relation $d = 6/\rho_t S_{BET}$. Given that the spherical particle approximation is poor for most powders anyway and provides no real benefits to the analysis, there seems to be no value in introducing it into the Thiele modulus.

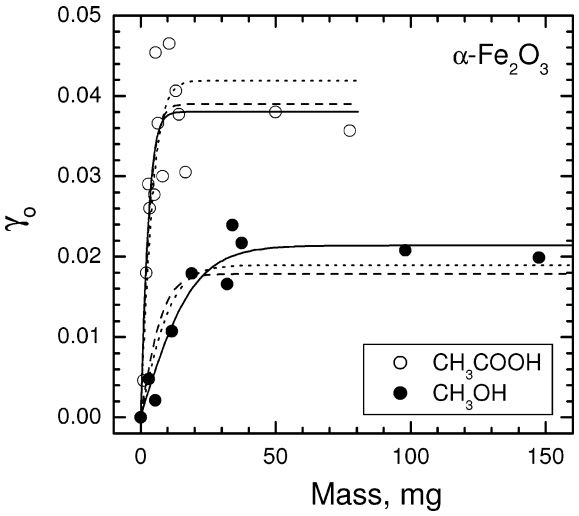

Figure 6. Knudsen cell data measured by Carlos-Cuellar et al.[59] for the initial uptake of acetic acid (CH_3COOH) and methanol (CH_3OH) on α-Fe_2O_3, fit by the KML model in different ways. Fitting information is listed in Table 6.

The large uncertainty in estimated effective diffusion coefficients reinforces the value of conducting experimental uptake measurements over as wide a range of sample masses (or bed depths) as possible, so that limiting uptake behaviors at extremes of the mass range are accessed. The use of only one of these limits remains problematic. For very small sample masses, where the powder bed depth approaches the roughness scale, it is unlikely that the underlying continuum formulation of the KML model remains valid. Thus, measurements must be made over a mass range where the minimum bed depth significantly exceeds the mean particle size but the maximum bed depth is not large enough for significant nonlinearity to appear in the slope of γ_o vs m. It may also be difficult to obtain an accurate slope $d\gamma_o/dm$ from a fit to the experimental data, especially for when γ_o increases rapidly with mass, as it will for efficient surface uptake reactions.

In the high mass limit, the evaluation of γ_t depends inversely on D_{eff} and to the second power on $\bar{\gamma}_o$. It appears that the accurate determination of $\bar{\gamma}_o$ has not received as much effort in the literature. However, if experimental values of both $\bar{\gamma}_o$ and $d\gamma_o/dm$ are available, one can combine eqs 9 and 10 to arrive at

$$D_{eff} = \frac{\bar{v}\bar{\gamma}_o^{\,2}}{4A_o\rho_b(d\gamma_o/dm)} \tag{24}$$

By inserting eq 24 into the Thiele modulus $\phi = (k/D_{eff})^{1/2}$, D_{eff} can be eliminated entirely from the KML procedure in favor of quantities measured during the uptake experiment.

Equation 24 can also be used to confirm that the experimental data is consistent with reasonable effective diffusion coefficient values. Within the approximation $r_p = 2\epsilon/\rho_b S_{BET}$, eq 24 can be solved further for tortuosity to give

$$\tau = \frac{16\epsilon^2 A_o(d\gamma_o/dm)}{3S_{BET}\bar{\gamma}_o^{\,2}} \tag{25}$$

For high porosity powder beds, the tortuosity computed by eq 25 should be small; values above 3 may reflect uncertainties in determining $d\gamma_o/dm$ and $\bar{\gamma}_o$ from the experimental measurements or deviations of the true diffusion-reaction phenomena from the KML model assumptions.

TABLE 6: KML Model Results for Figure 6

	fitting information		CH_3COOH		CH_3OH	
line	data sets	parameters	τ	γ_t, $\times 10^{-3}$	τ	γ_t, $\times 10^{-4}$
solid	individual	γ_t and τ	2.5 ± 0.6	1.9 ± 0.3	0.81 ± 0.22	1.9 ± 0.3
dashed [a]	simultaneous	γ_t and τ	2.2 ± 0.4	1.7 ± 0.3	2.2 ± 0.4	3.6 ± 0.9
dotted [b]	simultaneous	γ_t	1.5	1.4 ± 0.1	1.5	2.8 ± 0.6

[a] Single tortuosity as the fitting parameter. [b] Single tortuosity fixed at 1.5.

In one case reported by Underwood et al.,[31] an extremely large tortuosity of 195 used to fit the KML model to initial NO_2 uptake data on α-Al_2O_3 powder appears to result from a numerical error. By the use of values given in the text or extracted from the figures ($\epsilon = 0.85$, $A_o = 11.88$ cm^2, $S_{BET} = 140\,000$ cm^2 g^{-1}, $d\gamma_o/dm = 0.11$ g^{-1}, and $\bar{\gamma}_o = 0.0043$), eq 25 returns a much more reasonable value of $\tau = 1.9$.

In Figure 6, we have reproduced mass-dependent initial uptake coefficient data for acetic acid (CH_3COOH) and methanol (CH_3OH) on α-Fe_2O_3, as measured by Carlos-Cuellar et al.[59] using the Knudsen cell technique. Values given for various experimental parameters are $\rho_b = 2.1$ g cm^{-3}, $\rho_t = 5.24$ g cm^{-3}, $S_{BET} = 29\,000$ cm^2 g^{-1}, and $d = 0.69$ μm, with $A_o = 5.34$ cm^2 for the acetic acid experiments and $A_o = 5.07$ cm^2 for the methanol experiments. Using these values in the KML model fits produced $\gamma_t = (1.9 \pm 0.3) \times 10^{-3}$ with $\tau = 12$ for acetic acid and $\gamma_t = (1.9 \pm 0.4) \times 10^{-4}$ with $\tau = 3$ for methanol.[59] In their calculations, d was estimated from SEM images. If the individual data sets are refit letting the tortuosities vary freely and with $d = 6/\rho_t S_{BET} = 0.39$ μm, the fits produce similar values for the true uptake coefficients but with much lower values for tortuosity: $\tau = 2.5$ for acetic acid and $\tau = 0.81$ for methanol. These KML fits are shown as solid lines in Figure 6. The greatly reduced tortuosity value for the acetic acid experiment is much more in line with expected values, and while $\tau = 0.81$ is below 1 and therefore not physical, it is a fitting result compatible with the approximation $r_p = 2\epsilon/\rho_b S_{BET}$, as discussed above.

A further question arises: is it reasonable to extract two different tortuosity values for nominally identical powder beds in the two sets of experiments? If tortuosity is purely a geometric parameter it should be independent of the reactant gas. Even considering experimental variations in powder bed packing, the tortuosities should be more similar than the factor of 4 difference found in the analysis of Carlos-Cuellar et al. or the factor of 3.1 found here.

The dashed curves in Figure 6 show the KML model results if both data sets are fit simultaneously, with a single value of tortuosity allowed to vary freely. The resulting tortuosity is 2.2. The true uptake coefficient for the acetic acid experiments drops to 1.7×10^{-3}, a decrease of $\sim$10%. For the methanol experiment, the change is much bigger: a factor of 2 increase to 3.6×10^{-4}. From Figure 6, it is apparent that the KML model fit to the methanol data is significantly worse, in both the mass-dependent and independent regions. The dotted line in Figure 6 shows the KML results when the data sets are fit simultaneously with a single lower value of tortuosity fixed at 1.5; γ_t is now 25% lower than the initial fit for acetic acid and 47% larger than the initial fit for methanol. The fit to the methanol data is improved. The fit to the acetic acid data is now degraded but only in the mass-independent region where only two data points are available. Judging from the scatter in the acetic acid data measured for powder beds around 10 mg, it seems quite possible that the mass-independent asymptotic value $\bar{\gamma}_o$ is larger than that indicated by the two high mass data points.

This fitting exercise illustrates the dependence of the true uptake coefficients on choices made during the correction procedure, both in how KML parameter values are assigned and how the fitting procedure is constrained. The value of more extensive data in the mass-independent regime is reemphasized, since this ensures $\bar{\gamma}_o$ is experimentally well determined. For consistency with the definition of tortuosity as a strictly geometric descriptor, variations in tortuosity for the same nominal powder bed should be minimal. Simultaneous fitting of different reactant uptake data sets is a legitimate approach consistent with this viewpoint and, at least for this example, returns reasonable values for both uptake coefficients and tortuosity.

The use of low values of Knudsen diffusion coefficients or high values of tortuosity in the KML model to match experiment has sometimes been explained in terms of "sticky" behavior between reactants and surfaces.[31,65] While effective diffusivities extracted from transient uptake measurements can be greatly depressed by adsorption/desorption dynamics,[66] it is hard to rationalize a similar effect under steady-state conditions. The KML model is a steady-state model, wherein the effective diffusion coefficient describes the net transport of reactant molecules through the powder bed, not the transport of individual reactant molecules. The diffusive transport of individual molecules is described by their *tracer* diffusivity. Increased surface residence times will cause slower diffusion of individual molecules, however, the *transport* diffusivity which relates the net flux of molecules through the media under a steady-state concentration gradient is unaffected by surface residence time distributions.[67,68]

Given these considerations, in combination with experimental and simulation results for highly porous media, the use of the KML correction procedure in combination with large tortuosity values seems questionable for the powder beds typically used in heterogeneous atmospheric chemistry experiments. The need for high tortuosity values to fit KML models to experimental data is more likely to reflect limitations in particular experimental data sets or the constraints used in the fitting procedure or may indicate the presence of time-dependent processes that are not compatible with the steady-state KML formulation.

Finally, so long as the mass-dependent and mass-independent uptake regimes are well determined by experiment, and the tortuosity required to fit the KML model to the experimental data is reasonable (say $\tau \leq 3$), our results imply that it is not essential to measure Knudsen diffusion coefficients routinely during heterogeneous uptake experiments on the porous samples typically used in heterogeneous atmospheric chemistry experiments. Given the complexity and measurement uncertainty inherent in effective diffusion coefficient measurements, it seems unlikely that one could improve much on the uncertainty in γ_t that can be estimated by varying τ about its best-fit KML value within the $1 \leq \tau \leq 3$ range.

Acknowledgment. Funding for this work was provided by the NASA Geospace Sciences program through Grants NAG-512968 and NNG-05GJ71G and a joint CEDAR and NSF Atmospheric Chemistry postdoctoral fellowship ATM-0123118.

References and Notes

(1) Abbatt, J. P. D. *Chem. Rev.* **2003**, *103*, 4783.
(2) Quinlan, M. A.; Reihs, C. M.; Golden, D. M.; Tolbert, M. A. *J. Phys. Chem.* **1990**, *94*, 3255.
(3) Tolbert, M. A.; Rossi, M. J.; Golden, D. M. *Science* **1988**, *240*, 1018.
(4) Tolbert, M. A.; Rossi, M. J.; Malhotra, R.; Golden, D. M. *Science* **1987**, *238*, 1258.
(5) Grassian, V. H. *J. Phys. Chem. A* **2002**, *106*, 860.
(6) Rossi, M. J. *Chem. Rev.* **200**3, *103*, 4823.
(7) Gebel, M. E.; Finlayson-Pitts, B. J. *J. Phys. Chem. A* **2001**, *105*, 5178.
(8) Hoffman, R. C.; Gebel, M. E.; Fox, B. S.; Finlayson-Pitts, B. J. *Phys. Chem. Chem. Phys.* **2003**, *5*, 1780.
(9) Chu, L. T.; Leu, M.-T.; Keyser, L. F. *J. Phys. Chem.* **1993**, *97*, 7779.
(10) Keyser, L. F.; Moore, S. B.; Leu, M.-T. *J. Phys. Chem.* **1991**, *95*, 5496.
(11) Cooper, P. L.; Abbatt, J. P. D. *J. Phys. Chem.* **1996**, *100*, 2249.
(12) Jin, R.; Chu, L. T. *J. Phys. Chem. A* **2006**, *110*, 3647.
(13) Smith, W. V. *J. Chem. Phys.* **1943**, *11*, 110.
(14) Wise, H.; Ablow, C. M. *J. Chem. Phys.* **1958**, *29*, 634.
(15) Wise, H.; Wood, B. J. Reactive Collisions Between Gas and Surface Atoms. In *Advances in Atomic and Molecular Physics*; Bates, D. R., Estermann, I., Eds.; Academic Press: New York, 1967; Vol. 3, p 291.
(16) Wood, B. J.; Wise, H. *J. Chem. Phys.* **1958**, *29*, 1416.
(17) Kim, Y. C.; Boudart, M. *Langmuir* **1991**, *7*, 2999.
(18) Koch, T. G.; Fenter, F. F.; Rossi, M. J. *Chem. Phys. Lett.* **1997**, *275*, 253.
(19) Koch, T. G.; van den Bergh, H.; Rossi, M. J. *Phys. Chem. Chem. Phys.* **1999**, *1*, 2687.
(20) Alcala-Jornod, C.; van den Bergh, H.; Rossi, M. J. *Phys. Chem. Chem. Phys.* **2000**, *2*, 5584.
(21) Golden, D. M.; Spokes, G. N.; Benson, S. W. *Angew. Chem.* **1973**, *12*, 534.
(22) Caloz, F.; Fenter, F. F.; Rossi, M. J. *J. Phys. Chem.* **1996**, *100*, 7494.
(23) Fenter, F. F.; Caloz, F.; Rossi, M. J. *J. Phys. Chem.* **1994**, *98*, 9801.
(24) Fenter, F. F.; Rossi, M. J. *J. Phys. Chem. A* **1997**, *101*, 4110.
(25) Seisel, S.; Flückiger, B.; Caloz, F.; Rossi, M. J. *Phys. Chem. Chem. Phys.* **1999**, *1*, 2257.
(26) Hanisch, F.; Crowley, J. N. *Atmos. Chem. Phys.* **2003**, *3*, 119.
(27) Hanisch, F.; Crowley, J. N. *J. Phys. Chem. A* **200**1, *105*, 3096.
(28) Hanisch, F.; Crowley, J. N. *Phys. Chem. Chem. Phys.* **2001**, *3*, 2474.
(29) Hanisch, F.; Crowley, J. N. *Phys. Chem. Chem. Phys.* **2003**, *5*, 883.
(30) Underwood, G. M.; Li, P.; Al-Abadleh, H.; Grassian, V. H. *J. Phys. Chem. A* **2001**, *105*, 6609.
(31) Underwood, G. M.; Li, P.; Usher, C. R.; Grassian, V. H. *J. Phys. Chem.* **2000**, *104*, 819.
(32) Underwood, G. M.; Song, C. H.; Phadnis, M.; Carmichael, G. R.; Grassian, V. H. *J. Geophys. Res.* **2001**, *106*, 18055.
(33) Goodman, A. L.; Li, P.; Usher, C. R.; Grassian, V. H. *J. Phys. Chem. A* **2001**, *105*, 6109.
(34) Keyser, L. F.; Leu, M.-T. *J. Colloid Interface Sci.* **199**3, *155*, 137.
(35) Leu, M.-T.; Moore, S. B.; Keyser, L. F. *J. Phys. Chem.* **1991**, *95*, 7763.
(36) Wheeler, A. Reaction Rates and Selectivity in Catalyst Pores. In *Advances in Catalysis and Related Subjects*; Frankenburg, W. G., Rideal, E. K., Komarewsky, V. I., Eds.; Academic Press: New York, 1951; Vol. 3, p 249.
(37) Aris, R. *The Mathematical Theory of Diffusion and Reaction in Permeable Catalysts*; Clarendon Press: Oxford, U.K., 1975.
(38) Keyser, L. F.; Leu, M.-T.; Moore, S. B. *J. Phys. Chem.* **1993**, *97*, 2800.
(39) Thiele, E. W. *Ind. Eng. Chem.* **1939**, *31*, 916.
(40) Evans, R. B.; Watson, G. M.; Mason, E. A. *J. Chem. Phys.* **1961**, *35*, 2076.
(41) Scott, D. S.; Dullien, F. A. *AIChE J.* **1962**, *8*, 113.
(42) Remick, R. R.; Geankoplis, C. J. *Ind. Eng. Chem. Fundam.* **1973**, *12*, 214.
(43) Hirschfelder, J. O.; Curtiss, C. F.; Bird, R. B. *Molecular Theory of Gases and Liquids*; John Wiley & Sons: New York, 1967.
(44) Dullien, F. A. L.; Scott, D. S. *Chem. Eng. Sci.* **1962**, *17*, 771.
(45) Carman, P. C. *Flow of Gases Through Porous Media*; Butterworth Scientific Publications: London, 1956.
(46) Henry, J. P., Jr.; Cunningham, R. S.; Geankoplis, C. J. *Chem. Eng. Sci.* **1967**, *22*, 11.
(47) Marrero, T. R.; Mason, E. A. *Phys. Chem. Ref. Data* **1972**, *1*, 3.
(48) Dushman, S.; Lafferty, J. M. *Scientific Foundations of Vacuum Technique*, 2nd ed.; John Wiley and Sons: New York, 1962.
(49) Kennard, E. H. *Kinetic Theory of Gases*, 1st ed.; McGraw-Hill Book Company: New York, 1938.
(50) Masamune, S.; Smith, J. M. *AIChE J.* **1962**, *8*, 217.
(51) Wakao, N.; Smith, J. M. *Chem. Eng. Sci.* **1962**, *17*, 825.
(52) Rothfeld, L. B. *AIChE J.* **1963**, *9*, 19.
(53) Yu, A. B.; Feng, C. L.; Zou, R. P.; Yang, R. Y. *Powder Technol.* **2003**, *130*, 70.
(54) Boudreau, B. P. *Geochim. Cosmochim. Acta* **1996**, *60*, 3139.
(55) Abbasi, M. H.; Evans, J. W.; Abramson, I. S. *AIChE J.* **1983**, *29*, 617.
(56) Evans, J. W.; Abbasi, M. H.; Sarin, A. *J. Chem. Phys.* **198**0, *72*, 2967.
(57) Burganos, V. N. *J. Chem. Phys.* **1998**, *109*, 6772.
(58) Tomadakis, M. M.; Sotirchos, S. V. *AIChE J.* **1991**, *37*, 74.
(59) Carlos-Cuellar, S.; Li, P.; Christensen, A. P.; Krueger, B. J.; Burrichter, C.; Grassian, V. H. *J. Phys. Chem. A* **2003**, *107*, 4250.
(60) Johnson, E. R.; Sciegienka, J.; Carlos-Cuellar, S.; Grassian, V. H. *J. Phys. Chem. A* **2005**, *109*.
(61) Huizenga, D. G.; Smith, D. M. *AIChE J.* **1986**, *32*, 1.
(62) Olague, N.; Smith, D. M.; Ciftcioglu, M. *AIChE J.* **1988**, *34*, 1907.
(63) Wright, T.; Smith, D. S.; Stermer, D. L. *Ind. Eng. Chem. Res.* **1987**, *26*, 1227.
(64) Wang, C.-T.; Smith, J. M. *AIChE J.* **1983**, *29*, 132.
(65) Fenter, F. F.; Rossi, M. J. *J. Phys. Chem.* **1996**, *100*, 1008.
(66) Weisz, P. B. *Ind. Eng. Chem. Res.* **1995**, *34*, 2692.
(67) Malek, K.; Coppens, M.-O. *Phys. Rev. Lett.* **2001**, *87*, 125505.
(68) Malek, K.; Coppens, M.-O. *Colloids Surf., A* **2002**, *206*, 335.